ARTICLE

Effect of oxygen coordination environment of Ca-Mn oxides on catalytic performance of Pd supported catalysts for aerobic oxidation of 5-hydroxymethyl-2-furfural

Received 00th January 20xx,
Accepted 00th January 20xx

DOI: 10.1039/x0xx00000x

Jie Yang,[a,b,†] Haochen Yu,[a,b,†] Yanbing Wang,[b] Fuyuan Qi,[b] Haodong Liu,[b] Lan-Lan Lou,[b] Kai Yu,[a,*] Wuzong Zhou[c] and Shuangxi Liu[b,d]

Four types of Ca-Mn oxides, including $CaMnO_3$, $CaMn_2O_4$, $CaMn_3O_6$ and $Ca_2Mn_3O_8$, have been prepared and used as supports for Pd nanoparticles. The oxygen activation capacity of these oxides and the catalytic activity of the oxide supported Pd nanocatalysts have been investigated using the aerobic oxidation of 5-hydroxymethyl-2-furfural as a model reaction. It is found that the local coordination environment of lattice oxygen sites plays a crucial role on their redox property and charge transfer ability from Pd nanoparticles to the support. In particular, the Ca-Mn oxide with lower oxygen coordination number, weaker metal-oxygen bonds and tunnel crystal structure, e.g. $CaMn_2O_4$, exhibits promoted oxygen activation capacity, and stronger electron transfer ability. Consequently, Pd/$CaMn_2O_4$ exhibits the highest catalytic activity among these catalysts, providing a promising yield of 2,5-furandicarboxylic acid. This work may shed light on the future investigation on the design of local structure of active oxygen sites in oxides or oxide supported catalysts for redox reactions.

1. Introduction

To reveal the interplay between active site and catalytic activity at an atomic level is regarded as a huge challenge in the field of heterogeneous catalysis.[1] For the redox reactions on oxides, the catalytic cycle between adsorption and desorption of oxygenated species on active oxygen sites plays an important role in the redox property of the oxides.[2] Moreover, the oxygen adsorption and desorption processes occurred on oxide surface can directly promote the charge transfer ability in between the oxide and oxide supported metal particles, and result in the enhanced electronic metal–support interaction. However, to keep a balance of oxygen adsorption and desorption, two conflicting requirements, is critically important. The ability of catalytic cycle on these active oxygen sites should be relevant to many structural characteristics, such as the type of associated cations,[3,4] the coordination number,[5] and the intensity of metal-oxygen bonds.[6] Therefore, the deep insights into the relationship between local coordination environment of lattice oxygen in oxides and their reactivity can help us to tune the catalytic properties.

5-Hydroxymethyl-2-furfural (HMF), an important biomass platform chemical from dehydration of C_6-based carbohydrates, is a versatile precursor for multi-functional molecules with promising applications in production of fine chemicals, polymers and liquid fuels.[7,8] In particular, its selective catalytic oxidation has become a hot topic in the last decade. Many strategies have been reported for the oxidation of HMF, such as biological,[9] photocatalytic,[10,11] and electrochemical[12,13] oxidation processes. Compared with these methods, the aerobic oxidation of HMF catalyzed by oxides or oxide supported noble metal catalysts has received much more attention and been considered as a promising method for practical application.[14,15] Among the catalytic materials ever reported for this reaction, Mn-based oxides as catalysts[16-21] or catalyst supports[22] have recently attracted a great interest because of their low cost and superior performance.

The Ca-Mn mixed oxides are composed of inexpensive, environmentally friendly and highly abundant elements. Some of them can even be directly obtained from naturally occurring minerals, for example the marokite $CaMn_2O_4$. Their various crystal structures, such as spinel and perovskite, as well as the variable valence state of Mn make it convenient to tailor their physicochemical properties, and therefore, these oxides have been used in various heterogeneous catalytic systems.[23,24] However, to the best of our knowledge, Ca-Mn oxides have not been investigated in the aerobic oxidation of HMF. Furthermore, the variable crystal structure and Mn valence state also make Ca-Mn oxides an ideal substrate to study the effect of local coordination environment of lattice oxygen sites on their redox property and charge transfer ability.

[a] MOE Key Laboratory of Pollution Processes and Environmental Criteria, Tianjin Key Laboratory of Environmental Technology for Complex Transmedia Pollution, College of Environmental Science and Engineering, Nankai University, Tianjin 300350, China.
[b] Institute of New Catalytic Materials Science and MOE Key Laboratory of Advanced Energy Materials Chemistry, School of Materials Science and Engineering, National Institute of Advanced Materials, Nankai University, Tianjin 300350, China.
[c] School of Chemistry, University of St Andrews, Fife KY16 9ST, United Kingdom.
[d] Collaborative Innovation Center of Chemical Science and Engineering (Tianjin), Tianjin 300072, China
† These authors contributed equally to this work.
Electronic Supplementary Information (ESI) available: [details of any supplementary information available should be included here]. See DOI: 10.1039/x0xx00000x

Herein, we present our recent study on the synthesis of a series of Ca-Mn oxides with different compositions, such as $CaMnO_3$, $CaMn_2O_4$, $CaMn_3O_6$ and $Ca_2Mn_3O_8$, which were used as supports for Pd nanoparticles. The obtained catalysts were evaluated in the aerobic oxidation of HMF towards 2,5-furandicarboxylic acid (FDCA). Through experimental and theoretical investigations, the influence of the crystal structures of Ca-Mn oxides, including the local coordination environments of lattice oxygen, on the catalytic activity and charge transfer ability was studied in detail. Among these Ca-Mn oxides, $CaMn_2O_4$ exhibited the highest redox properties and oxygen activation capacity. It can provide more active oxygen species to react with spilled H atoms that were generated from the dehydrogenation of HMF on Pd, and thus significantly improve the overall catalytic performance of $Pd/CaMn_2O_4$ for aerobic oxidation of HMF. The reason for the excellent catalytic property relating to the microstructures of the active sites is discussed. We believe that this work may shed light on the future study about the structure-activity relationship of active oxygen sites in oxides or oxide supported metal catalysts for catalytic oxidation reactions.

2. Experimental Section

2.1 Materials

Potassium chloride (KCl), palladium chloride ($PdCl_2$), manganese nitrate [$Mn(NO_3)_2$, 50 wt% in H_2O], anhydrous calcium carbonate ($CaCO_3$), concentrated nitric acid (HNO_3), phosphoric acid (H_3PO_4), ethylene glycol and polyvinylpyrrolidone (PVP) were obtained from Aladdin. Ammonium bicarbonate (NH_4HCO_3) and ammonium carbonate [$(NH_4)_2CO_3$] were supplied by Kewei Chemical Industry Co., Ltd. HMF and FDCA were purchased from Heowns Biochemical Technology Co., Ltd. 5-Hydroxymethyl-2-furancarboxylic acid (HMFCA) was provided by Matrix Scientific. 2,5-Diformylfuran (DFF) and 5-formyl-2-furancarboxylic acid (FFCA) were obtained from Sun Chemical Technology Co., Ltd and Toronto Research Chemicals Inc., respectively. These chemicals were used as-received without further purification.

2.2 Characterization

Powder X-ray diffraction (XRD) was performed on a Bruker D8 FOCUS diffractometer (Cu K_α radiation) with a scanning rate of 0.2º/s. X-ray photoelectron spectroscopy (XPS) was conducted using a Kratos Axis Ultra DLD spectrometer employing a monochromatic Al K_α X-ray source (hν = 1486.6 eV). High resolution spectra from some relevant binding energy (BE) ranges were recorded, calibrated using the C 1s peak (BE = 284.6 eV) of carbon contaminants as an internal standard. A JEOL JSM-7500F field-emission scanning electron microscope (SEM) and an FEI Tecnai G2 F20 transmission electron microscope (TEM) were used to detect the morphological and structural features of the specimens. O_2-TPD, H_2-TPR, O_2-TPO measurements and pulse CO chemisorption experiments were performed on a Micromeritics ChemiSorb 2750 analyzer with a thermal conductivity detector. In O_2 temperature-programmed desorption (O_2-TPD) experiments, 100 mg of the sample was pretreated in O_2 at 100 °C, same as the reaction temperature of aerobic oxidation of HMF, for adsorption for 60 min. In H_2 temperature-programmed reduction (H_2-TPR) experiments, 100 mg of the sample was heated from 25 °C to 800 °C at a rate of 10 °C/min under 5% H_2/Ar flow (25 mL/min). In O_2 temperature-programmed oxidation (O_2-TPO) experiments, 100 mg of the sample was pretreated in 5% H_2/Ar at 600 °C for 60 min, cooled down to 25 °C, and then heated to 800 °C at a rate of 10 °C/min under 5% O_2/He flow (25 mL/min). In pulse CO chemisorption experiments, pulses of 10% CO/He were introduced to the catalyst at 25 °C until three successive peaks showed the same peak area. A CO/Pd stoichiometry of 1 was used for calculation of surface Pd amount.[25] Brunauer-Emmett-Teller (BET) surface areas were estimated from the N2 adsorption-desorption isotherms at the liquid-nitrogen temperatures using a Micromeritics ASAP 2020 physisorption instrument. Prior to N_2 adsorption, 100 mg of the sample was degassed under N_2 flow at 180 °C for 8 h. The contents of Ca, Mn and Pd were detected by inductively coupled plasma atomic emission spectrometry (ICP-AES) on an IRIS Intrepid II XSP instrument from Thermo Fisher Scientific Inc.

2.3 Synthesis of Ca-Mn oxides

Ca-Mn oxides were prepared through a thermal decomposition method using $Ca_nMn_{1-n}CO_3$ solid solution precursors according to a reported method.[26] In a typical process, fresh $MnCO_3$ was precipitated from a solution containing $Mn(NO_3)_2$ and NH_4HCO_3. Then the stoichiometric $MnCO_3$ and $CaCO_3$ were dissolved in a 0.5 M dilute HNO_3 solution and, to this solution was added an excess solution of $(NH_4)_2CO_3$ ($CO_3^{2-}/(Ca^{2+}+Mn^{2+})$ molar ratio = 5) under vigorous stirring. After further stirring for 30 min, the $Ca_nMn_{1-n}CO_3$ precursor was collected by centrifugation, washing with water and vacuum-drying. The Ca-Mn oxides with nominal compositions of $Ca_xMn_yO_z$ (x:y = 1:1, 1:2, 1:3, 2:3) were then obtained by calcination of the precursor in a muffle furnace. The calcination conditions for the target compounds were as follows: $CaMnO_3$ (900 °C, 5 h), $CaMn_2O_4$ (950 °C, 10 h), $CaMn_3O_6$ (800 °C, 1 h), $Ca_2Mn_3O_8$ (700 °C, 1 h). The actual Mn/Ca molar ratios in the products were determined by ICP-AES, which are 0.99 for $CaMnO_3$, 2.04 for $CaMn_2O_4$, 3.11 for $CaMn_3O_6$, and 1.52 for $Ca_2Mn_3O_8$, respectively. The measured elemental contents of Ca and Mn in the $Ca_xMn_yO_z$ oxides show good matching to the nominal compositions.

2.4 Synthesis of Ca-Mn oxide supported Pd catalysts

$PdCl_2$ and KCl (K/Pd molar ratio = 2) were dissolved in water under stirring. Then a desired amount of $Ca_xMn_yO_z$ was added and the resulting suspension was stirred continuously for 12 h. These samples were reduced by ethylene glycol aqueous solution that containing a small amount of PVP at 130 °C for 4 h. Finally, the solid sample was collected by centrifuging, washing repeatedly with water and ethanol, and vacuum-drying. During this process, we expect that Pd nanoclusters deposit on the surface of the oxide particles, and can then be designated as

$Pd/Ca_xMn_yO_z$. The nominal mass percentage of Pd in these catalysts is 1.0 wt%. The actual Pd loadings on these catalysts detected by ICP-AES were 0.88 wt%, 0.92 wt%, 0.93 wt%, and 0.90 wt% for $Pd/CaMnO_3$, $Pd/CaMn_2O_4$, $Pd/CaMn_3O_6$, and $Pd/Ca_2Mn_3O_8$, respectively.

2.5 Aerobic oxidation of HMF

A certain amount of catalyst (0.016 mmol of Pd) was added to a 10 mL of HMF aqueous solution (40 mmol/L). The reaction solution was refluxed at 100 °C and bubbled with O_2 flow under stirring. Then 50 μL of sample was taken out from the reaction solution when needed for examination, diluted to 5 mL with water, and filtered by a 0.2 μm PTFE membrane. The concentrations of HMF and its derivatives were detected by Agilent 1200 series high-performance liquid chromatography (HPLC) equipped with a Sepax Carbomix H-NP10:8% column (column temperature: 65 °C) and an ultraviolet-visible detector operating at 271 nm using an external standard curve method. A H_3PO_4 aqueous solution (1 mmol/L) was used as mobile phase with a flow rate of 0.6 mL/min. The relative standard deviation (RSD) values of the yield of products were determined by four parallel experiments as lower than 2.5%.

2.6 Computational methods

The density functional theory (DFT) calculations were performed using the projector augmented-wave (PAW)[27,28] method as implemented in the Vienna ab initio simulation package (VASP) code[29]. All energy calculations were performed within the generalized gradient approximation (GGA-PW91)[30]. An energy cutoff of 400 eV was used for the plane-wave expansion of the electronic wave function. The on-site coulomb and exchange interactions in the localized d orbital electrons of Mn by adding an effective Hubbard-U parameter to repulse electrons on the same orbitals. It was reported that the theoretical U and J values were 5.0 and 1.0 eV[31,32], respectively. In these DFT+U calculations, the most stable surfaces of $Ca_xMn_yO_z$ samples were referred to the XRD analysis, which were (121) for $CaMnO_3$, (023) for $CaMn_2O_4$, (021) for $CaMn_3O_6$, and (020) for $Ca_2Mn_3O_8$ with top two atomic layers relaxed and bottom four layers fixed. The corresponding k-points of $CaMnO_3$(121), $CaMn_2O_4$(023), $CaMn_3O_6$(021), $Ca_2Mn_3O_8$(020) were set to 2 × 1 × 1, 6 × 1 × 1, 2 × 1 × 1, and 2 × 1 × 1, respectively. The vacuum space was set to 20 Å between the slabs to minimize their interaction.

3. Results and Discussion

3.1 Characterization of samples

Fig. 1 depicts the XRD patterns of the as-synthesized four types of $Ca_xMn_yO_z$ compounds. The diffraction peaks of these oxides can be perfectly indexed to orthorhombic perovskite structure of $CaMnO_3$ (JCPDS 76-1132), orthorhombic post-spinel structure of $CaMn_2O_4$ (JCPDS 70-4889), monoclinic post-spinel structure of $CaMn_3O_6$ (JCPDS 31-0285) and monoclinic layered structure of $Ca_2Mn_3O_8$ (JCPDS 73-2290), indicating a successful preparation of four monophasic Ca-Mn oxides.

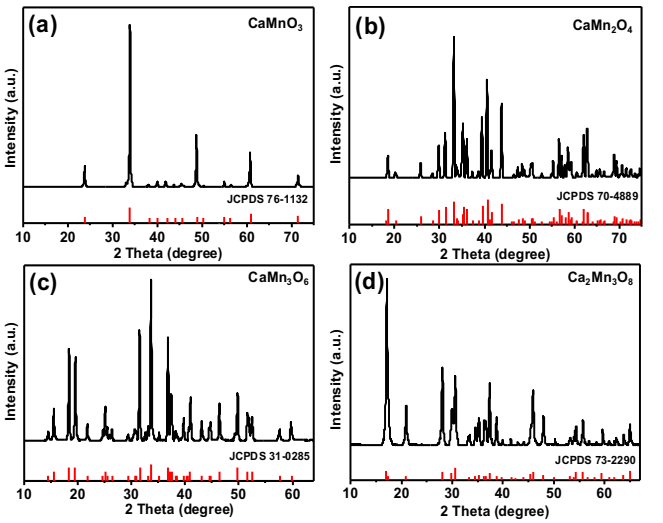

Fig. 1. XRD patterns of the as-synthesized $Ca_xMn_yO_z$ samples with standard patterns. (a) Orthorhombic $CaMnO_3$ with a = 5.278, b = 7.459, and c = 5.273 Å. (b) Orthorhombic $CaMn_2O_4$ with a = 3.153, b = 9.977, and c = 9.665 Å. (c) Monoclinic $CaMn_3O_6$ with a = 10.592, b = 11.327, c = 8.453 Å and β = 121.45°. (d) Monoclinic $Ca_2Mn_3O_8$ with a = 11.004, b = 5.837, c = 4.938 Å and β = 109.72°.

Fig. 2a-d are SEM images of the obtained $Ca_xMn_yO_z$ samples, showing a similar porous walnut shape with the diameters in a range of 1.0 to 2.8 μm, although their structures fall into four quite different types. The corresponding low magnification SEM images showing many particles are presented in Fig. S1a-d. The $CaMnO_3$ and $CaMn_2O_4$ spheres consist of granular particles with a size of ca. 100 nm. The $CaMn_3O_6$ spheres consist of nanorods with 300-400 nm in length and 100 nm in width. The formation of nanorod morphology can be explained by the tunnel structure of $CaMn_3O_6$, which is based on a framework of double chains of edge-sharing MnO_6 octahedra propagating along c-axis.[33] The $Ca_2Mn_3O_8$ spheres are formed by intergrowth of nanoparticles,

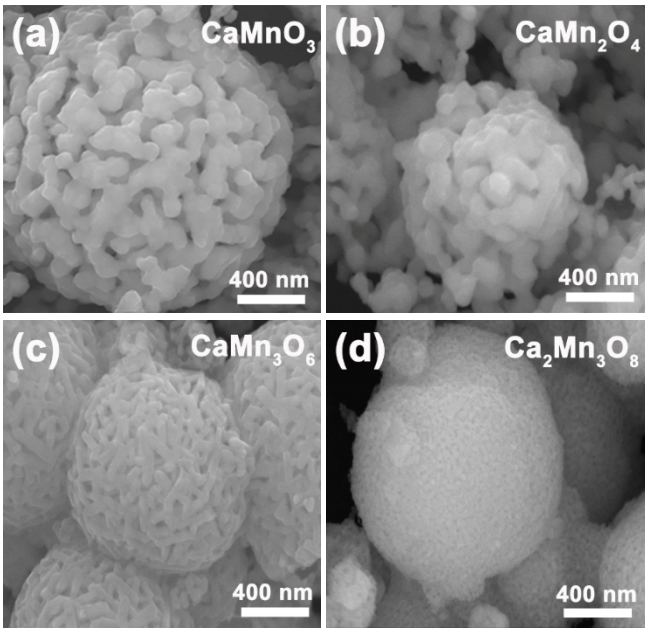

Fig. 2. SEM images of the as-synthesized $Ca_xMn_yO_z$ samples.

20-70 nm in diameter. The walnut morphology of these spherical particles were not resulted from aggregation of small crystallites, but inherited from a spherical-like morphology of the $Ca_nMn_{1-n}CO_3$ precursors (as shown in Fig. S2). When the carbonates decomposed into oxides, the volume of the materials shrank to form a network-like porous structure. The BET surface areas of these $Ca_xMn_yO_z$ samples were measured to be 64 m^2/g for $CaMnO_3$, 72 m^2/g for $CaMn_2O_4$, 79 m^2/g for $CaMn_3O_6$, and 88 m^2/g for $Ca_2Mn_3O_8$, respectively.

After deposition of Pd nanoparticles on the $Ca_xMn_yO_z$ particles, the resulting catalysts were characterized by TEM as shown in Fig. 3. It can be found that Pd nanoparticles are evenly dispersed on the surface of the oxide particles, and the average diameters of Pd nanoparticles range from 3.0 nm to 3.3 nm, as measured from more than 200 particles for each sample. Figs. 3e-h show the high resolution TEM (HRTEM) images of the synthesized $Pd/Ca_xMn_yO_z$ catalysts. The measured d-spacings on the polycrystalline oxide substrates can be indexed to the (121) planes of $CaMnO_3$, (131) planes of $CaMn_2O_4$, (320) and (140) planes of $CaMn_3O_6$, and (111), (020) and (-201) planes of $Ca_2Mn_3O_8$, respectively. The d-spacings of 0.23 and 0.22 nm can be ascribed to the (111) planes of the cubic Pd structure. In addition, it can be seen from the HRTEM images that the grains or nanorods as shown in SEM images (Fig. 2) are not single crystals of Ca-Mn oxides. The domain structures can be observed in these oxides.

In order to investigate the chemical state of the obtained $Ca_xMn_yO_z$ samples and $Pd/Ca_xMn_yO_z$ catalysts, XPS characterizations in Mn 3s, Mn 2p, and O 1s regions for $Ca_xMn_yO_z$ and in Pd 3d region for $Pd/Ca_xMn_yO_z$ were carried out and the results are shown in Fig. 4. The Mn 3s XPS spectra were recorded to analyze the mean valence states of Mn in $Ca_xMn_yO_z$ samples because the energy separation of the splitting of Mn 3s peaks has a linear relationship to Mn valence.[34] Based on Fig. 4a, the mean valence states of Mn were established at +3.98, +2.83, +3.43, and +3.89 for $CaMnO_3$, $CaMn_2O_4$, $CaMn_3O_6$ and $Ca_2Mn_3O_8$, respectively. The Mn oxidation states in $CaMnO_3$, $CaMn_2O_4$, and $Ca_2Mn_3O_8$ are slightly lower than the nominal values (+4, +3, and +4 for $CaMnO_3$, $CaMn_2O_4$, and $Ca_2Mn_3O_8$, respectively), which can be derived from the existence of surface oxygen vacancies generated in the calcination process. However, the mean valence state of Mn in $CaMn_3O_6$ is obviously higher than the nominal value (+10/3), which can be explained by the partial leaching of Ca cations from $CaMn_3O_6$ resulting in the rise of the valence state of Mn because of the charge compensation. Indeed, a higher ratio (3.11) of Mn/Ca was detected in the ICP-AES result for $CaMn_3O_6$. $CaMn_2O_4$ exhibits the biggest difference in Mn valence state between the measured value (+2.83) and the nominal value (+3), suggesting the largest amount of oxygen vacancies in $CaMn_2O_4$.

To further investigate the chemical state of Mn, the Mn 2p XPS spectra (Fig. 4b) of the obtained $Ca_xMn_yO_z$ samples were recorded. The Mn 2p peaks were deconvoluted into several sub-bands derived from Mn^{2+}, Mn^{3+}, and Mn^{4+}. The molar percentage of Mn cations with different valence states were calculated and listed in Table 1. It can be seen that the distribution of Mn cations with different valence states in these $Ca_xMn_yO_z$ samples is well consistent with the results obtained from Mn 3s XPS spectra. More specifically, $CaMn_2O_4$ possesses the largest amount of relative low-valence Mn cations compared with their nominal valence. $CaMn_3O_6$ shows relatively higher percentage of Mn^{4+} (50.5%) compared with the nominal value (33.3%). In addition, about 10-15% of low-valence Mn cations (Mn^{3+}) can be observed in $Ca_2Mn_3O_8$ and $CaMnO_3$.

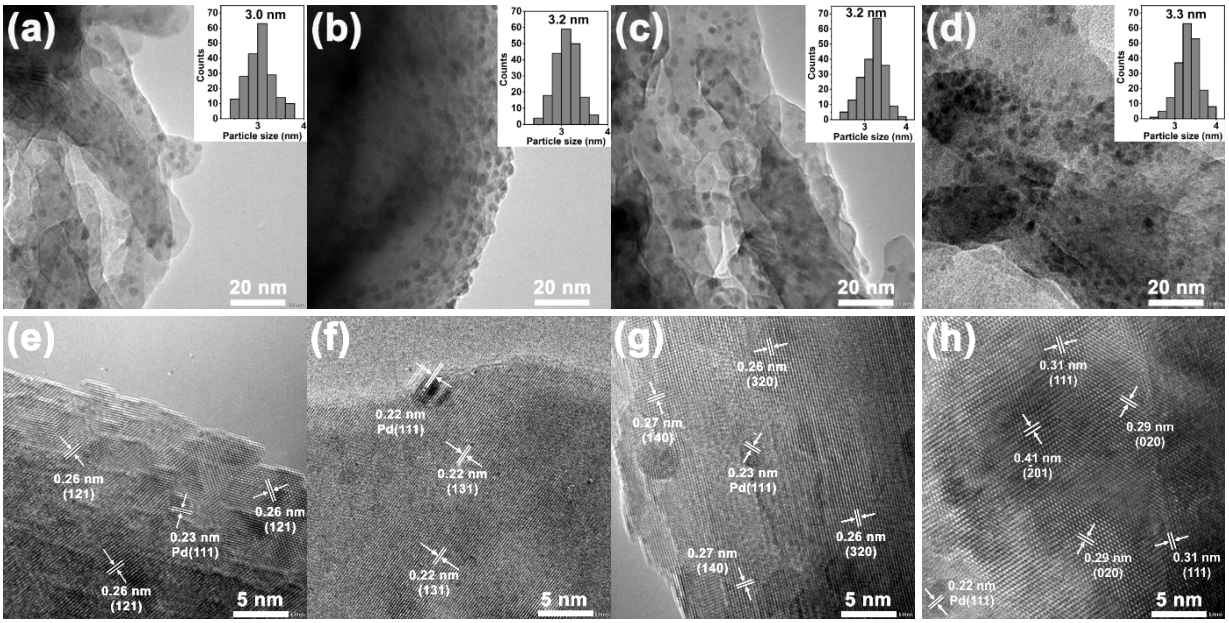

Fig. 3. TEM and HRTEM images of the obtained (a,e) $Pd/CaMnO_3$, (b,f) $Pd/CaMn_2O_4$, (c,g) $Pd/CaMn_3O_6$ and (d,h) $Pd/Ca_2Mn_3O_8$ catalysts with some measured d-spacings. The insets in a-d are the corresponding Pd particle size distributions.

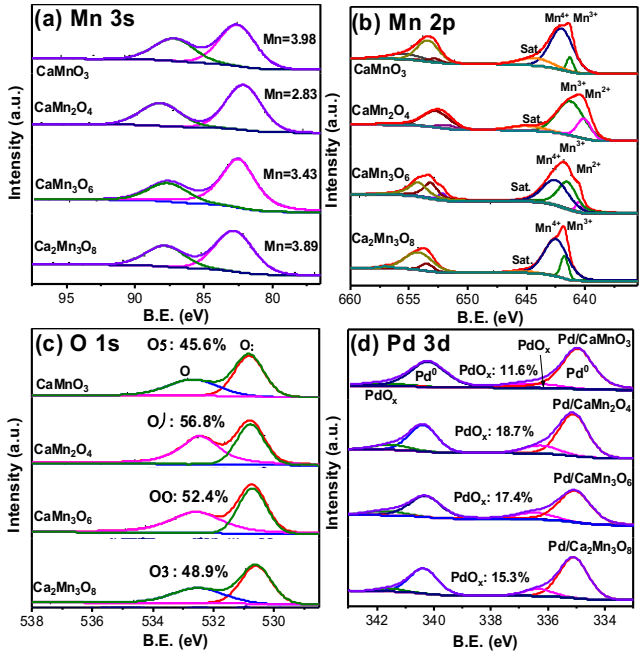

Fig. 4. XPS spectra in the regions of (a) Mn 3s, (b) Mn 2p and (c) O 1s of $Ca_xMn_yO_z$, and (d) Pd 3d of Pd/$Ca_xMn_yO_z$.

For these Ca-Mn oxides, more lattice oxygen vacancies would lead to higher activity for reversible reaction of surface Mn species with O_2.[35] Thus, the O 1s XPS of $Ca_xMn_yO_z$ samples were detected to investigate the surface oxygen species (see Fig. 4c). The deconvoluted O 1s peaks show two components at ~530.6 eV (O_β) and ~532.5 eV (O_α) that arise from lattice oxygen (O^{2-}) and surface chemisorbed oxygen species (e.g. O_2^- and O_2^{2-}), respectively.[4] The relative abundance of O_α component in the surface regions of the $Ca_xMn_yO_z$ samples were calculated to be 45.6% for $CaMnO_3$, 56.8% for $CaMn_2O_4$, 52.4% for $CaMn_3O_6$, and 48.9% for $Ca_2Mn_3O_8$, respectively. Since the origin of O_α component is related to the oxygen vacancies in these oxides, the higher relative abundance of O_α component indicates more oxygen vacancies and higher oxygen activation capacity. The O 1s XPS characterization results suggest that $CaMn_2O_4$ has the highest oxygen activation capacity among these $Ca_xMn_yO_z$ samples, which is consistent with the results of Mn 3s XPS characterization. The order of oxygen activation capacity of these $Ca_xMn_yO_z$ samples determined by O 1s XPS characterization is $CaMn_2O_4$ > $CaMn_3O_6$ > $Ca_2Mn_3O_8$> $CaMnO_3$.

Table 1. The molar percentage of Mn cations with different valence states in $Ca_xMn_yO_z$ samples calculated from the Mn 2p XPS spectra

Sample	Molar percentage of Mn cations (%)		
	Mn^{2+}	Mn^{3+}	Mn^{4+}
$CaMnO_3$	–	10.3	89.7
$CaMn_2O_4$	23.1	76.9	–
$CaMn_3O_6$	5.1	44.4	50.5
$Ca_2Mn_3O_8$	–	15.7	84.3

After deposition of Pd nanoparticles, the chemical states of Pd in Pd/$Ca_xMn_yO_z$ catalysts were studied by Pd 3d XPS (Fig. 4d). The Pd 3d peaks can be deconvoluted to two states, the metallic Pd^0 state and the surface oxidized PdO_x state.[36,37] The formation of PdO_x species can be attributed to the air exposure of the catalysts[38] and should be also related to the oxygen activation capacity of the $Ca_xMn_yO_z$ samples.[39] Among these Pd/$Ca_xMn_yO_z$ catalysts, Pd/$CaMn_2O_4$ exhibits the highest amount of PdO_x species. It can also be found from Fig. 4d, the Pd 3d binding energy of Pd^0 species in Pd/$CaMn_2O_4$ is obviously higher than those in Pd/$CaMnO_3$, suggesting the lower electron density of Pd in Pd/$CaMn_2O_4$. Moreover, the Mn 3s XPS spectra of Pd/$Ca_xMn_yO_z$ (Fig. S3) indicates an obvious decrease in the mean valance state of Mn of Pd/$Ca_xMn_yO_z$ after the deposition of Pd. The XPS results suggest that an electron transfer from Pd to support occurs in Pd/$Ca_xMn_yO_z$.[40] In order to further prove that, the Bader charge analysis of Pd4 cluster on $CaMn_2O_4$ (Fig. S4) has been carried out, an electropositive Bader valence of Pd atoms (-0.7 |e|) was obtained, which confirmed the electron transfer from Pd to the support. It has been reported that the $Pd^{\delta+}$ species should be beneficial to the adsorption of electronegative reactants and the dehydrogenation of alcohol and aldehyde groups of HMF.[41] Thus, it becomes necessary to further study the oxygen activation capacity of these Ca-Mn oxides.

As shown in Fig. 5a, the O_2-TPD profiles of $Ca_xMn_yO_z$ samples exhibited two desorption peaks centered at 294-340 °C and 630-665 °C, which can be attributed to the desorption of chemically adsorbed oxygen species, such as O_2^- and O_2^{2-},[42,43] and the desorption of surface lattice oxygen atoms, respectively. It can be seen that $CaMn_2O_4$ possesses the lowest desorption temperature of O_2 in both temperature regions, indicating that the active oxygen species and surface lattice oxygen atoms are more inclined to desorb from $CaMn_2O_4$ than from the other $Ca_xMn_yO_z$ samples. The order of the O_2 desorption temperature of these $Ca_xMn_yO_z$ samples follows $CaMn_2O_4$ < $CaMn_3O_6$ < $Ca_2Mn_3O_8$ < $CaMnO_3$. The relative amounts of O_2-TPD in the range of 294-340 °C were calculated, which are 126 μmol/g for $CaMnO_3$, 160 μmol/g for $Ca_2Mn_3O_8$, 193 μmol/g for $CaMn_3O_6$ and 233 μmol/g for $CaMn_2O_4$, respectively. It can be seen that among these $Ca_xMn_yO_z$ samples, $CaMn_2O_4$ exhibits the highest relative amount in low temperature region, suggesting the highest oxygen adsorption capacity. Moreover, the order of oxygen adsorption capacity of $Ca_xMn_yO_z$ determined by O_2-TPD is well consistent with the results obtained from O 1s XPS.

To investigate the redox property of these $Ca_xMn_yO_z$ samples, H_2-TPR (Fig. 5b) and O_2-TPO (Fig. 5c) experiments were carried out. As shown in Fig. 5b, two groups of H_2 consumption peaks can be observed centered at ca. 396-472 °C and 543-613 °C, which can be attributed to the oxygen removal from the redox sites with different chemical environments. $CaMn_2O_4$ exhibits the lowest reduction temperatures (ca. 396 °C and 543 °C) and the lowest initial reduction temperature (131 °C) among these $Ca_xMn_yO_z$ samples, suggesting the highest reducibility of the redox sites in $CaMn_2O_4$. Perovskite structured $CaMnO_3$ exhibits the highest reduction temperatures, implying the lowest

reducibility. The order of the reducibility follows $CaMn_2O_4$ > $CaMn_3O_6$ > $Ca_2Mn_3O_8$ > $CaMnO_3$.

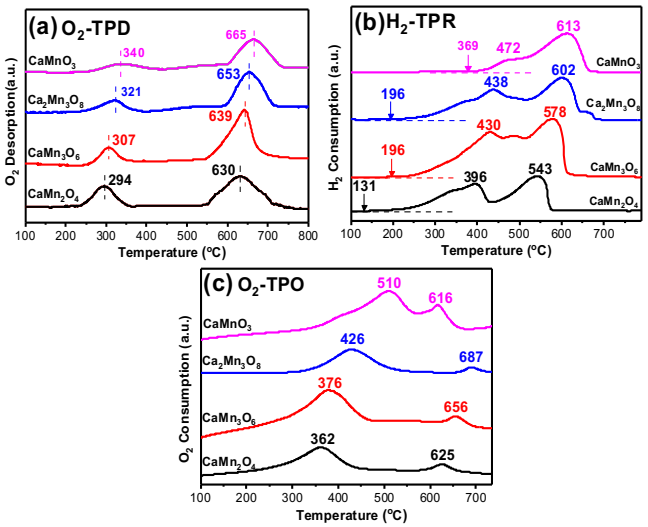

Fig. 5. The (a) O_2-TPD, (b) H_2-TPR, and (c) O_2-TPO results of the $Ca_xMn_yO_z$ samples.

The oxidizability of these $Ca_xMn_yO_z$ samples were evaluated by the O_2-TPO experiments (Fig. 5c). All the samples show two oxidation peaks centered at 362-510 °C and 616-687 °C, which can be associated with the oxidation processes of the reduced redox sites in $Ca_xMn_yO_z$ samples. The oxidation peaks at low temperature regions (<600 °C) are more prominent, suggesting the major oxidation process. Similarly, $CaMn_2O_4$ shows the lowest oxidation temperature at this region, indicating the best oxidizability compared with the other $Ca_xMn_yO_z$ samples. The order of the oxidation temperature of these $Ca_xMn_yO_z$ samples is $CaMn_2O_4$ < $CaMn_3O_6$ < $Ca_2Mn_3O_8$ < $CaMnO_3$. It is interesting that among these $Ca_xMn_yO_z$ samples, $CaMn_2O_4$ exhibits the highest oxygen adsorption capacity and the best redox property, implying the highest catalytic performance of $CaMn_2O_4$ in a redox reaction. After the deposition of Pd nanoparticles, the obtained Pd/$CaMn_2O_4$ exhibits further enhanced oxygen activation capacity and redox property based on the O_2-TPD, H_2-TPR and O_2-TPO experiments (Fig. S5). Even though the dehydrogenation reaction of HMF are considered to take place on the surface of Pd nanoparticles, the redox property and O_2 activation ability of reducible oxide support are still regarded to play an important role in aerobic oxidation of HMF.[3,22] Therefore, the influences of crystal structure and the local structure of oxygen active sites of these $Ca_xMn_yO_z$ samples on their redox property would be discussed in detail in the following section.

Influence of crystal structure of $Ca_xMn_yO_z$ on their redox property

Fig. 6 shows the crystal structures of obtained $Ca_xMn_yO_z$ samples. Perovskite structured $CaMnO_3$ consists of a framework with corner-sharing MnO_6 octahedra (Fig. 6a). Ca^{2+} cations locate at A sites (12 coordinated) of the perovskite structure.[31,44] $CaMn_2O_4$ and $CaMn_3O_6$ with a post-spinel structure (Fig. 6b and 6c) are composed of edge-sharing MnO_6 octahedral double chains. The angularly connected double chains with corner-sharing form a six-sided tunnel for storing Ca^{2+}.[45,46] In the tunnel of $CaMn_3O_6$, about one third of the Ca^{2+} sites are vacant, which is equivalent to $Ca_{2/3}Mn_2O_4$.[33] $Ca_2Mn_3O_8$ with a monoclinic layered structure can be thought as comprising of co-edge MnO_6 layers separated by Ca^{2+} cations.[47]

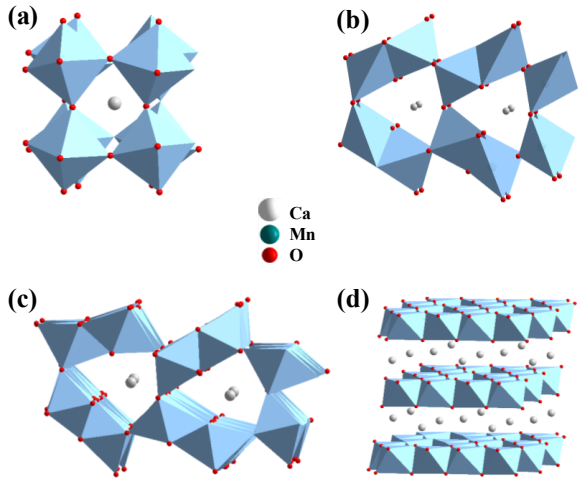

Fig. 6. Schematic crystal structures of (a) $CaMnO_3$, (b) $CaMn_2O_4$, (c) $CaMn_3O_6$, and (d) $Ca_2Mn_3O_8$.

From crystal structure point of view, the hexagonal-sided tunnels in $CaMn_2O_4$ and $CaMn_3O_6$ provide a unique space for the accommodation of Ca^{2+}, at the same time, the tunnels in a fixed direction are favourable for the entrance and adsorption of oxygen.[32] Similarly, the layer structure of $Ca_2Mn_3O_8$ can also promote the adsorption of oxygen due to the large interlayer space. On the contrary, the relatively dense structure of perovskite structured $CaMnO_3$ would restrict the diffusion of oxygen and the mobility of oxygen atoms. In addition, according to the results of theoretical calculation for the adsorption of O_2 molecule on the surface of $Ca_xMn_yO_z$ samples by Han et al.,[26] molecular O_2 is bound to low coordinated surface Mn cations of $CaMnO_3$, $CaMn_3O_6$ and $Ca_2Mn_3O_8$ via a lateral Griffith (side-on) manner, favouring a dissociation of the O-O bond into two O atoms to fill the adjacent vacancies. While, the molecular O_2 is bound to the surface of $CaMn_2O_4$ via a Pauling (end-on) manner to 5 coordinated Mn cations, tending to be reduced to active oxygen species. Therefore, among these $Ca_xMn_yO_z$ oxides, $CaMn_2O_4$ exhibited the highest oxygen activation ability. Combined with the results of O1s XPS and O_2-TPD characterizations, the oxygen adsorption and activation ability of these $Ca_xMn_yO_z$ samples should follow the order that post-spinel structure > monoclinic layered structure > perovskite structure.

The reactivity of surface lattice oxygen in these Ca-Mn oxides can be investigated through DFT calculations. The oxygen vacancy formation energy, $E_f(Ov)$, a commonly used descriptor of the reducibility of surface lattice oxygen with different coordination environments was calculated through the formula $E_f(Ov) = E_{def} - E_{free} + ½ E_{O2}$, in which E_{def}, E_{free}, and E_{O2} are the energies of the defective structure with an oxygen vacancy, the perfect system, and the free molecular oxygen, respectively.[48] Fig. 7 describes the surface chemical status of these $Ca_xMn_yO_z$ samples. The surface lattice oxygen atoms with relatively low

coordination numbers of metal cations are highlighted and the calculated E_f(Ov) values of these lattice oxygen atoms have been given.

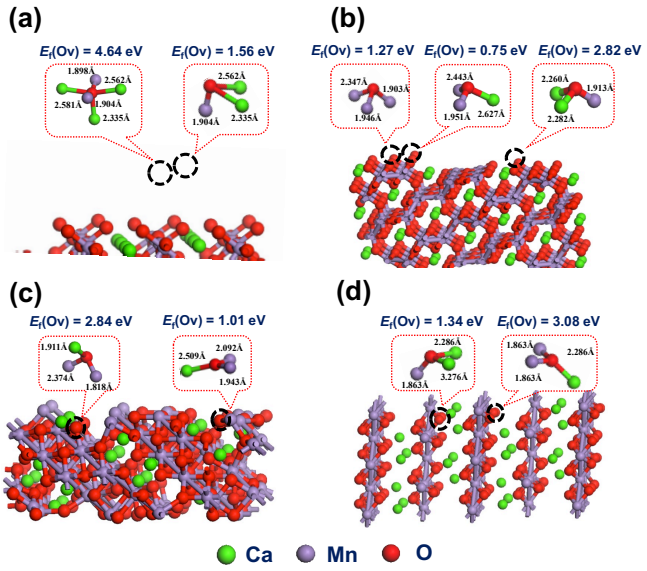

Fig. 7. The coordination status of surface lattice oxygen atoms and their calculated Ef(Ov) values in (a) $CaMnO_3$, (b) $CaMn_2O_4$, (c) $CaMn_3O_6$, and (d) $Ca_2Mn_3O_8$, showing the relevant bond lengths of Mn-O and Ca-O.

It can be seen from Fig. 7, the 3 coordinated surface lattice oxygen atoms of these $Ca_xMn_yO_z$ samples exhibit lower E_f(Ov) values, suggesting the higher reducibility of oxygen atoms, compared with those with higher coordination number (e.g. 5 in Fig. 7a). Among these lattice oxygen atoms with 3-fold coordination, the oxygen atoms associated with two Mn cations and one Ca cation in $CaMn_2O_4$ exhibited the lowest E_f(Ov) value (0.75 eV, Fig. 7b), which can be attributed to the relatively longer bond lengths of Ca-O (2.627 Å) and Mn-O (2.443 Å), indicating the highest reducibility of lattice oxygen in $CaMn_2O_4$. The lowest E_f(Ov) value of 3 coordinated lattice oxygen in $CaMn_3O_6$ is 1.01 eV, coming from an oxygen associated with two Mn cations and one Ca cation (Fig. 7c). The lattice oxygen atoms associated with two Ca cations and one Mn cation possessed the lowest E_f(Ov) values in $CaMnO_3$ and $Ca_2Mn_3O_8$ (Fig. 7a, d), which are 1.56 eV for $CaMnO_3$ and 1.34 eV for $Ca_2Mn_3O_8$. The order of the reducibility of surface lattice oxygen atoms determined by DFT calculations is $CaMn_2O_4$ > $CaMn_3O_6$ > $Ca_2Mn_3O_8$ > $CaMnO_3$, which are consistent with the results of H_2-TPR experiments. Through the DFT investigation, the rules can be found that the surface lattice oxygen with lower coordination number and longer M-O bond length would exhibit the higher reducibility.

Aerobic oxidation of HMF

The catalytic performance of the obtained $Pd/Ca_xMn_yO_z$ catalysts was evaluated in aerobic oxidation of HMF and the results are shown in Fig. 8. It can be clearly seen that, among these as-synthesized catalysts, $Pd/CaMn_2O_4$ exhibits the highest catalytic performance. Full conversion of HMF was achieved at 3 h and 96.8% yield of FDCA was obtained at 12 h with a carbon balance of 98.0%. Compared with ever reported catalysts,[49-52] the catalytic activity and selectivity of $Pd/CaMn_2O_4$ are considered as a promising result. For the other $Pd/Ca_xMn_yO_z$ catalysts, full conversion of HMF was achieved for at least 6 h, and the highest yield of FDCA at 12 h was 78.8% obtained over $Pd/CaMn_3O_6$. Among them, $Pd/CaMnO_3$ exhibited the lowest catalytic activity, and only 57.3% yield of FDCA was obtained after 12 h reaction.

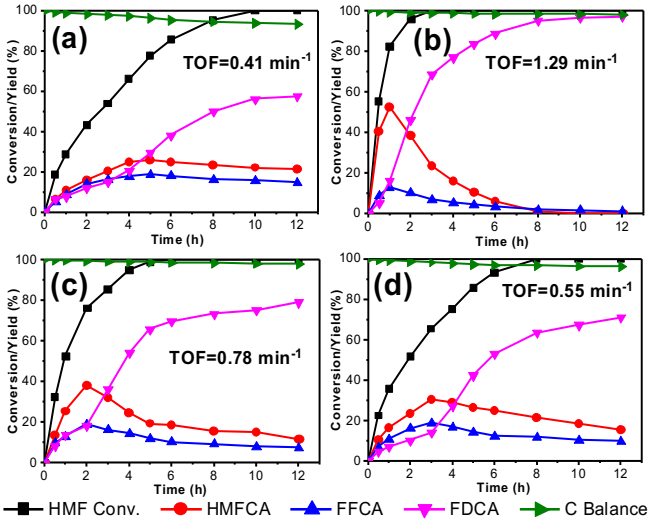

Fig. 8. The catalytic performance of (a) $Pd/CaMnO_3$, (b) $Pd/CaMn_2O_4$, (c) $Pd/CaMn_3O_6$, and (d) $Pd/Ca_2Mn_3O_8$. Reaction conditions: HMF 40 mmol/L, H_2O 10 mL, n_{HMF}/n_{Pd} = 25, n_{Na2CO3}/n_{HMF}(mol/mol) = 2, 100 °C, O_2 bubbling (100 mL/min)

In order to compare the catalytic activities more quantitatively, turnover frequency (TOF) values of $Pd/Ca_xMn_yO_z$ for aerobic oxidation of HMF were calculated based on the conversion of HMF at 30 min using the following equation (1). The Pd dispersion data of these $Pd/Ca_xMn_yO_z$ catalysts were determined by pulse CO chemisorption experiments, which are 37.9 % for $Pd/CaMnO_3$, 35.7% for $Pd/CaMn_2O_4$, 34.4% for $Pd/CaMn_3O_6$, and 33.8% for $Pd/Ca_2Mn_3O_8$, respectively. The calculated TOF values are given in Fig. 8. It is interesting to note that the order of catalytic performance of $Pd/Ca_xMn_yO_z$ catalysts is well consistent with the order of oxygen activation capacity and that of charge transfer ability from Pd to $Ca_xMn_yO_z$ support.

$$TOF(min^{-1}) = \frac{Conv_{HMF}(\%) \times (n_{HMF}/n_{Pd})}{time(min) \times Pd\ dispersion} \quad (1)$$

Reusability of $Pd/Ca_xMn_yO_z$ catalysts

The stability and reusability of $Pd/CaMn_2O_4$ catalyst were studied through successive recycling tests under the same reaction conditions. After each cycling experiment, the catalyst was collected by centrifugation, washing with deionized water several times and drying under vacuum at 50 °C. The reaction time of each cycling experiment was fixed to 12 h. The yield of FDCA can reach up to 96.8% for the 1st run. HMF in these cycling experiments was all fully converted. It can be found from Fig. 9a, in the first three cycling experiments, the yield of FDCA was slightly decreased from 96.8% for the 1st run to 89.8% for the 3rd run, suggesting a slight deactivation of $Pd/CaMn_2O_4$.

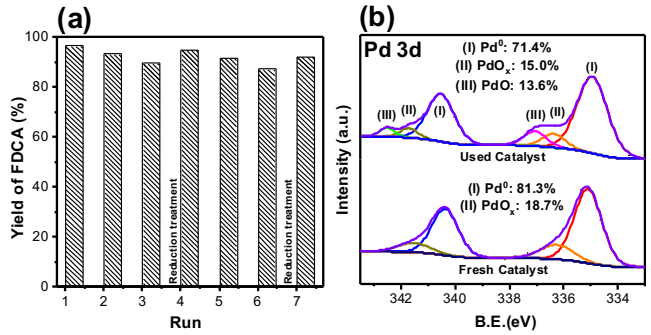

Fig. 9. (a) Recycling tests of $Pd/CaMn_2O_4$ for the aerobic oxidation of HMF. Reaction conditions: HMF 40 mmol/L, H_2O 10 mL, n_{HMF}/n_{Pd} = 25, n_{Na2CO3}/n_{HMF} (mol/mol) = 2, 100 °C, O_2 bubbling (100 mL/min), 12 h. (b) Pd 3d XPS spectra of fresh and used (after three cycling experiments) $Pd/CaMn_2O_4$ catalysts.

In order to reveal the reason of the slight deactivation, the element contents of used $Pd/CaMn_2O_4$ catalyst was detected by ICP-AES. Negligible Pd leaching (0.08%) was observed after three cycling experiments. Then, the used $Pd/CaMn_2O_4$ catalyst was detected by XPS in Pd 3d region, and the recorded spectra is shown in Fig. 9b. Compared with the fresh catalyst, the used catalyst exhibited a couple of new peaks located at 337.1 and 342.5 eV derived from Pd $3d_{5/2}$ and $3d_{3/2}$, respectively, which can be attributed to the surface PdO phase.[36,37] As shown in Fig. 9b, about 13.6% of Pd atoms are oxidized after three cycling experiments, which should be the main reason for catalyst deactivation. In order to prove this, the used $Pd/CaMn_2O_4$ catalyst was treated through an ethylene glycol reduction process, and then used in the next cycling experiment. Notably increased yield of FDCA (95.2%) can be achieved in the 4th run compared with that in the 3rd run. Similarly, when the yield of FDCA obviously decreased in the sixth cycling experiment, a reduction treatment can regenerate the catalyst and 92.4% yield of FDCA can be achieved at the following cycling experiment. Therefore, the decline in catalyst activity in cycling experiments can be mainly attributed to the partial oxidation of Pd nanoparticles, which might be derived from the enhanced oxygen activation capacity and electron transfer ability from Pd to $CaMn_2O_4$. Through a facilitated reduction treatment, the catalytic activity can be restored to its initial potential.

Promoting mechanism of $Pd/Ca_xMn_yO_z$ catalyst for aerobic oxidation of HMF

As mentioned previously, the Pd nanocatalyst supported on $CaMn_2O_4$ that had the highest oxygen activation capacity and charge transfer ability exhibited the highest catalytic activity in aerobic oxidation of HMF. According to the dehydrogenation mechanism of HMF over noble metal catalysts proposed by Davis et al.,[52] the metallic Pd is the primary active site for the dehydrogenation of HMF. The H atoms left on Pd nanoparticles react with O_2 to generate H_2O. When the oxide supports were more reactive for activation of O_2, the generated active oxygen species should react with spilled H atoms, making the reduction of O_2 occur on the oxide supports instead of Pd nanoparticles. It will leave more Pd active sites available for the dehydrogenation of HMF. In addition, the O_2 activation process on the support can consume electrons and provide a driving force of electron transfer from Pd to support.[3] The produced $Pd^{\delta+}$ species can significantly promote the dehydrogenation reactions of HMF on the surface of Pd nanoparticles. Based on these results and discussions, the reaction mechanism of aerobic oxidation of HMF over $Pd/CaMn_2O_4$ is proposed and described in Fig. 10.

The six-step dehydrogenation reactions from HMF to FDCA take place on the surface of Pd nanoparticles and leave H atoms on Pd surface (Scheme S1).[53] One part of H atoms can react with adsorbed OH^- to generate H_2O and e^-, and another part of H atoms will spill to the surface of $CaMn_2O_4$.[54,55] Because of the excellent reducibility of surface lattice oxygen in $CaMn_2O_4$, the spilled H atoms can react with the active oxygen species near the metal-oxide interface and leave the oxygen vacancies. At the same time, the adsorption and activation processes of O_2 occur on the oxygen vacancy sites of $CaMn_2O_4$ to generate the chemisorbed oxygen species (e.g. O_2^- and O_2^{2-}) or lattice oxygen species (O^{2-}). Owing to the excellent ability of catalytic cycle of oxygen adsorption and desorption on the active sites of $CaMn_2O_4$, the synergistic catalytic process presented on $CaMn_2O_4$ can significantly promote the catalytic performance of $Pd/CaMn_2O_4$ catalyst in aerobic oxidation of HMF.

Conclusions

In summary, four types of $Ca_xMn_yO_z$ oxides have been prepared and used as supports for Pd nanoparticles. Through experimental and theoretical investigation, the effect of crystal structure, including local coordination environment of lattice oxygen, on the oxygen activation capacity of $Ca_xMn_yO_z$ and charge transfer ability from Pd nanoparticles to the supports have been studied. Among these $Ca_xMn_yO_z$ oxides, post-spinel structured $CaMn_2O_4$ exhibited the highest oxygen activation capacity. It can be attributed to its tunnel crystal structure, promoting the adsorption and activation of molecular O_2, as well as to the relatively lower coordination number and longer M-O bonds of surface lattice oxygen, resulting in the higher reducibility of surface lattice oxygen. The promoted oxygen activation capacity of $CaMn_2O_4$ would lead to the enhanced charge transfer from Pd nanoparticles to the support, and thus improved catalytic activity for aerobic oxidation of HMF towards FDCA. Consequently, $Pd/CaMn_2O_4$ exhibited the highest catalytic activity. Finally, the reaction mechanism over $Pd/CaMn_2O_4$ catalyst was proposed. We believe that this work can provide insights into the structure-activity relationship of active oxygen sites in oxides or oxide supported metal catalysts, where the catalytic cycle between adsorption and desorption of oxygen atoms took place.

Conflicts of interest

There are no conflicts to declare.

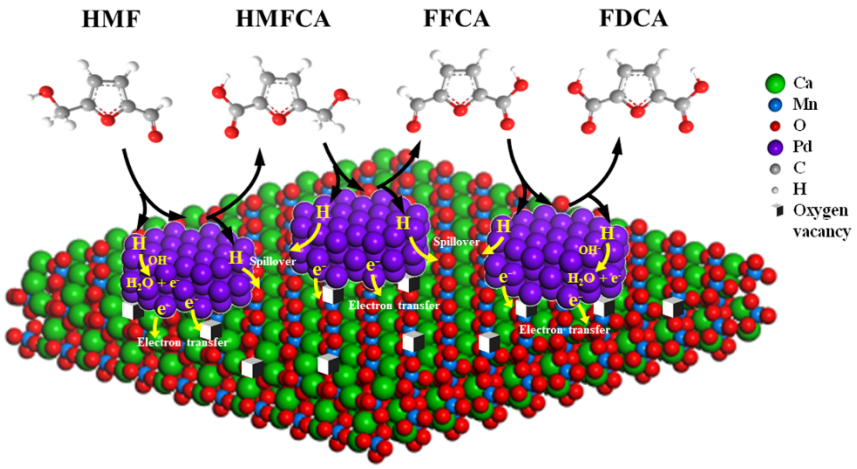

Fig. 10. Proposed promoting mechanism on Pd/$CaMn_2O_4$ for aerobic oxidation of HMF.

Acknowledgements

This work was supported by Natural Science Foundation of Tianjin (Grant No. 17JCYBJC22600) and the Fundamental Research Funds for the Central Universities. Computational support was provided by the Beijing Computing Center (BCC).

References

1. Y. Sun, S. Gao, F. Lei and Y. Xie, *Chem. Soc. Rev.*, 2015, **44**, 623-636.
2. E. W. McFarland and H. Metiu, *Chem. Rev.*, 2013, **113**, 4391-4427.
3. K. Yu, D. Lei, Y. Feng, H. Yu, Y. Chang, Y. Wang, Y. Liu, G.-C. Wang, L.-L. Lou, S.X. Liu and W.Z. Zhou, *J. Catal.*, 2018, **365**, 292-302.
4. K. Yu, Y. Liu, D. Lei, Y. Jiang, Y. Wang, Y. Feng, L.-L. Lou, S.X. Liu and W.Z. Zhou, *Catal. Sci. Technol.*, 2018, **8**, 2299-2303.
5. V. Fung, F. F. Tao and D.-E. Jiang, *J. Phys. Chem. Lett.*, 2017, **8**, 2206-2211.
6. V. Fung, Z. Wu and D.-E. Jiang, *J. Phys. Chem. Lett.*, 2018, **9**, 6321-6325.
7. Z. Mou and E. Y. X. Chen, *ACS Sustain. Chem. Eng.*, 2016, **4**, 7118-7129.
8. I. Delidovich, P. J. C. Hausoul, L. Deng, R. Pfützenreuter, M. Rose and R. Palkovits, *Chem. Rev.*, 2016, **116**, 1540-1599.
9. W. P. Dijkman, D. E. Groothuis and M. W. Fraaije, *Angew. Chem. Int. Ed.*, 2014, **53**, 6515-6518.
10. S. Xu, P. Zhou, Z. Zhang, C. Yang, B. Zhang, K. Deng, S. Bottle and H. Zhu, *J. Am. Chem. Soc.*, 2017, **139**, 14775-14782.
11. I. Krivtsov, E. I. García-López, G. Marcì, L. Palmisano, Z. Amghouz, J. R. García, S. Ordóñez and E. Díaz, *Appl. Catal. B: Environ.*, 2017, **204**, 430-439.
12. W.-J. Liu, L. Dang, Z. Xu, H.-Q. Yu, S. Jin and G. W. Huber, *ACS Catal.*, 2018, **8**, 5533-5541.
13. B. You, N. Jiang, X. Liu and Y. Sun, *Angew. Chem. Int. Ed.*, 2016, **55**, 9913-9917.
14. Z. Zhang and K. Deng, *ACS Catal.*, 2015, **5**, 6529-6544.
15. Z. Zhang and G. W. Huber, *Chem. Soc. Rev.*, 2018, **47**, 1351-1390.
16. E. Hayashi, Y. Yamaguchi, K. Kamata, N. Tsunoda, Y. Kumagai, F. Oba and M. Hara, *J. Am. Chem. Soc.*, 2019, **141**, 890-900.
17. E. Hayashi, T. Komanoya, K. Kamata and M. Hara, *ChemSusChem*, 2017, **10**, 654-658.
18. X. Han, C. Li, X. Liu, Q. Xia and Y. Wang, *Green Chem.*, 2017, **19**, 996-1004.
19. M. Ventura, F. Nocito, E. de Giglio, S. Cometa, A. Altomare and A. Dibenedetto, *Green Chem.*, 2018, **20**, 3921-3926.
20. K. T. V. Rao, J. L. Rogers, S. Souzanchi, L. Dessbesell, M. B. Ray and C. Xu, *ChemSusChem*, 2018, **11**, 3323-3334.
21. F. Neațu, R. S. Marin, M. Florea, N. Petrea, O. D. Pavel and V. I. Pârvulescu, *Appl. Catal. B: Environ.*, 2016, **180**, 751-757.
22. T. Gao, J. Chen, W. Fang, Q. Cao, W. Su and F. Dumeignil, *J. Catal.*, 2018, **368**, 53-68.
23. M. M. Najafpour, T. Ehrenberg, M. Wiechen and P. Kurz, *Angew. Chem. Int. Ed.*, 2010, **49**, 2233-2237.
24. F. Rong, J. Zhao, Z. Chen, Y. Xu, Y. Zhao, Q. Yang and C. Li, *J. Mater. Chem. A*, 2016, **4**, 6585-6594.
25. C. Zhang, Y. Li, Y. Wang and H. He, *Environ. Sci. Technol.*, 2014, **48**, 5816-5822.
26. X. Han, T. Zhang, J. Du, F. Cheng and J. Chen, *Chem. Sci.*, 2013, **4**, 368-376.
27. P. E. Blöchl, *Phys. Rev. B*, 1994, **50**, 17953-17979.
28. G. Kresse and J. Furthmüller, *Comp. Mater. Sci.*, 1996, **6**, 15-50.
29. G. Kresse and J. Furthmüller, *Phys. Rev. B*, 1996, **54**, 11169-11186.
30. J. P. Perdew and Y. Wang, *Phys. Rev. B*, 1992, **45**, 13244-13249.
31. M. Molinari, D. A. Tompsett, S. C. Parker, F. Azough and R. Freer, *J. Mater. Chem. A*, 2014, **2**, 14109-14117.

32. M. E. A.-D. Dompablo, C. Krich, J. Nava-Avendaño, N. Biškup, M. R. Palacín and F. Bardé, *Chem. Mater.*, 2016, **28**, 6886-6893.
33. J. Hadermann, A. M. Abakumov, L. J. Gillie, C. Martin and M. Hervieu, *Chem. Mater.*, 2006, **18**, 5530-5536.
34. M. Toupin, T. Brousse and D. Bélanger, *Chem. Mater.*, 2004, **16**, 3184-3190.
35. V. D. Makwana, Y.-C. Son, A. R. Howell and S. L. Suib, *J. Catal.*, 2002, **210**, 46-52.
36. G. Ketteler, D. F. Ogletree, H. Bluhm, H. Liu, E. L. D. Hebenstreit and M. Salmeron, *J. Am. Chem. Soc.*, 2005, **127**, 18269-18273.
37. M. Peuckert, *J. Phys. Chem.*, 1985, **89**, 2481-2486.
38. J. An, G. Sun and H. Xia, *ACS Sustain. Chem. Eng.*, 2019, **7**, 6696-6706.
39. Y. Chen, H. Zheng, Z. Guo, C. Zhou, C. Wang, A. Borgna and Y. Yang, *J. Catal.*, 2011, **283**, 34-44.
40. G. Sun, J. An, H. Hu, C. Li, S. Zuo and H. Xia, *Catal. Sci. Technol.*, 2019, **9**, 1238-1244.
41. Y. Wang, K. Yu, D. Lei, W. Si, Y. Feng, L.-L. Lou and S.X. Liu, *ACS Sustain. Chem. Eng.*, 2016, **4**, 4752-4761.
42. Y. Meng, W. Song, H. Huang, Z. Ren, S.-Y. Chen and S. L. Suib, *J. Am. Chem. Soc.*, 2014, **136**, 11452-11464.
43. V. P. Santos, M. F. R. Pereira, J. J. M. Órfão and J. L. Figueiredo, *Appl. Catal. B: Environ.*, 2010, **99**, 353-363.
44. G. Zhang, G. Liu, L. Wang and J. T. S. Irvine, *Chem. Soc. Rev.*, 2016, **45**, 5951-5984.
45. T. Yang, M. Croft, A. Ignatov, I. Nowik, R. Cong and M. Greenblatt, *Chem. Mater.*, 2010, **22**, 5876-5886.
46. J. Du, Y. Pan, T. Zhang, X. Han, F. Cheng and J. Chen, *J. Mater. Chem.*, 2012, **22**, 15812-15818.
47. L. J. Vera Stimpson, E. E. Rodriguez, C. M. Brown, G. B. G. Stenning, M. Jura and D. C. Arnold, *J. Mater. Chem. C*, 2018, **6**, 4541-4548.
48. J. Yang, C.-Q. Lv, Y. Guo and G.-C. Wang, *J. Chem. Phys.*, 2012, **136**, 104107.
49. P. V. Rathod and V. H. Jadhav, *ACS Sustain. Chem. Eng.*, 2018, **6**, 5766-5771.
50. C. Chen, X. Li, L. Wang, T. Liang, L. Wang, Y. Zhang and J. Zhang, *ACS Sustain. Chem. Eng.*, 2017, **5**, 11300-11306.
51. Z. Zhang, J. Zhen, B. Liu, K. Lv and K. Deng, *Green Chem.*, 2015, **17**, 1308-1317.
52. N. Mei, B. Liu, J. Zheng, K. Lv, D. Tang and Z. Zhang, *Catal. Sci. Technol.*, 2015, **5**, 3194-3202.
53. S. E. Davis, B. N. Zope and R. J. Davis, *Green Chem.*, 2012, **14**, 143-147.
54. L. R. Baker, G. Kennedy, M. van Spronsen, A. Hervier, X. Cai, S. Chen, L.-W. Wang and G. A. Somorjai, *J. Am. Chem. Soc.*, 2012, **134**, 14208-14216.
55. L. Zhu, Y. Jiang, J. Zheng, N. Zhang, C. Yu, Y. Li, C.-W. Pao, J.-L. Chen, C. Jin, J.-F. Lee, C.-J. Zhong and B. H. Chen, *Small*, 2015, **11**, 4385-4393.

The Table of Contents (TOC)

Effect of oxygen coordination environment of Ca-Mn oxides on catalytic performance of Pd supported catalysts for aerobic oxidation of 5-hydroxymethyl-2-furfural

Jie Yang, Haochen Yu, Yanbing Wang, Fuyuan Qi, Haodong Liu, Lan-Lan Lou, Kai Yu*, Wuzong Zhou, and Shuangxi Liu

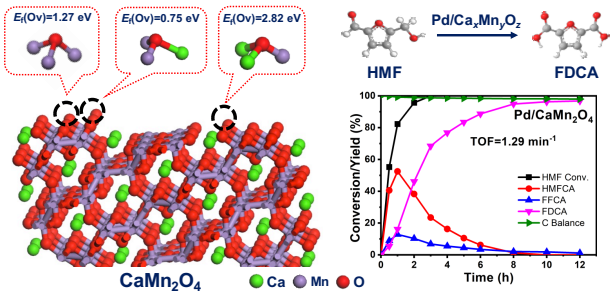

$Pd/CaMn_2O_4$ provides ideal active sites for oxygen adsorption and desorption, resulting in the promoted charge transfer ability and catalytic activity.